Chemical Science

ROYAL SOCIETY OF CHEMISTRY

EDGE ARTICLE

View Article Online
View Journal | View Issue

Cite this: *Chem. Sci.*, 2025, **16**, 2316

All publication charges for this article have been paid for by the Royal Society of Chemistry

Received 17th October 2024
Accepted 25th December 2024

DOI: 10.1039/d4sc07077a

rsc.li/chemical-science

Hollow core–shell heterojunction TAPB-COF@$ZnIn_2S_4$ as highly efficient photocatalysts for carbon dioxide reduction†

Huitao Fan, * Minglin Hu, Yabing Duan, Luyang Zuo, Ronggui Yu, Zhuwei Li, Qi Liu, Bo Li * and Liya Wang

The conversion of carbon dioxide (CO_2) into carbon-neutral fuels using solar energy is crucial for achieving energy sustainability. However, the high carrier charge recombination and low CO_2 adsorption capacity of the photocatalysts present significant challenges. In this paper, a TAPB-COF@$ZnIn_2S_4$-30 (TAPB-COFZ-30) heterojunction photocatalyst was constructed by *in situ* growth of $ZnIn_2S_4$ (ZIS) on a hollow covalent organic framework (HCOF) with a hollow core–shell structure for CO_2 to CO conversion. Both experimental studies and theoretical calculations indicate that the construction of heterojunctions improves the efficiency of carrier separation and utilisation in photocatalysis. The yield of photoreduction of CO_2 to CO by the TAPB-COFZ-30 heterojunction photocatalyst reached 2895.94 μmol g^{-1} with high selectivity (95.75%). This study provides a feasible strategy for constructing highly active core–shell composite photocatalysts to optimize CO_2 reduction.

Introduction

Dependence on the combustion of fossil fuels to meet energy needs has resulted in the accumulation of large quantities of greenhouse gases in the atmosphere, which has serious environmental consequences; thus, reducing the use of fossil fuels and improving the use of clean energy are the energy challenges we face today.[1–5] Among the many clean energy sources, the utilisation of solar energy has been widely recognized. The use of semiconductors as catalysts for the photoreduction of CO_2 into valuable chemical substances is an innovative green technology, which is considered one of the most promising solutions for reducing CO_2 emissions, both in terms of solving the environmental challenges created by the greenhouse effect and alleviating the problem of energy scarcity.[6–11] Semiconductors were reported for CO_2 photocatalytic reduction at the end of the twentieth century.[12] Although most of the photocatalysts have achieved relatively good results, there are still some problems, such as limited visible light collection, poor selectivity for the desired products, poor utilization of photon-generated carriers, and other problems.[4,13–16]

In recent years, among various semiconductor materials, the transition metal sulfide photocatalyst ZIS has attracted great interest by virtue of its suitable electronic energy band structure, good chemical stability, low toxicity and facile preparation.[16–19] However, the photocatalytic activity of ZIS still fails to meet the requirements for a wider range of applications due to the fast recombination and low mobility of light-induced electron–hole pairs.[20,21] Its excessive self-assembly ability also reduces its specific surface area and active sites.[22] Therefore, it is necessary to find stable and reliable substrate materials to inhibit the self-loading of ZIS, and optimize the charge separation/transfer and CO_2 adsorption capabilities of ZIS photocatalysts to achieve more efficient CO_2 conversion. In recent years, an emerging class of visible light-responsive porous crystalline materials, covalent organic frameworks (COFs), has attracted much attention due to their abundant porosity, structural diversity, high thermal stability, and low density.

The benefits of COFs are as follows: (1) compared with traditional inorganic or organic semiconductors, their high surface area and plentiful nitrogen atom framework provide higher adsorption capacity and CO_2 selectivity; (2) improved thermal and chemical stability; (3) regular crystal structure and uniform channel distribution, reduced charge recombination, enhanced mass transfer ability, *etc.*[9,23–26] The adsorption performance of COFs on CO_2 has been greatly improved with the rapid development of research since their first report in 2009.[27] Considering these advantages, COF materials can be used as ideal components coupled with ZIS to construct composite photocatalysts. Among the reported COF materials, nitrogen-rich COFs such as TAPB are expected to be excellent candidates for CO_2 capture owing to the increased affinity of nitrogen atoms for interacting with CO_2.[28]

College of Chemistry and Pharmaceutical Engineering, Nanyang Normal University, Nanyang, 473601, P. R. China. E-mail: fanhuitao818@nynu.edu.cn; libony0107@nynu.edu.cn

† Electronic supplementary information (ESI) available. See DOI: https://doi.org/10.1039/d4sc07077a

Therefore, in this work, the nitrogen-rich TAPB-COF was synthesized from 1,3,5-tris(4-aminophenyl)benzene (TAPB) and 2,5-diethenyl-1,4-benzenedicarboxaldehyde (DVA), and the hollow core–shell photocatalyst TAPB-COF@ZIS was constructed by a one-step hydrothermal method for the photocatalytic reduction of CO_2. The CO_2 reduction mechanism was revealed by *in situ* Fourier transform infrared spectroscopy (*in situ* FTIR) and Gibbs free energy calculations. X-ray photoelectron spectroscopy (XPS) and theoretical calculations show that the carrier migration and separation processes in TAPB-COF@ZIS follow a type-II transfer mechanism. Photoelectrochemical tests and N_2, CO_2 adsorption results showed that the incorporation of TAPB-COF promoted the separation and transport of photogenerated carriers, increased the specific surface area of ZIS and CO_2 adsorption. This unique photocatalyst, TAPB-COFZ-30, has the optimal TAPB-COF content, with higher photocatalytic activity than that of the original ZIS (about 6 folds) and TAPB-COF (about 33 folds). This work highlights the potential application of ZIS-based photocatalysts for CO_2 photoreduction. Furthermore, it provides a new strategy for the design of COF@ZIS composite materials, and further lays a foundation for the development of CO_2 reduction photocatalysts.

Experimental section

Materials

Hydrogen peroxide (H_2O_2) was purchased from Tianjin Fengchuan Chemical Reagent Co., Ltd. *N*′*N*-Dimethylformamide (DMF), acetonitrile (MeCN), ethanol, and acetic acid (HAc), were purchased from Tianjin Comieo Chemical Reagent Co., Ltd. 1,3,5-Tris(4-aminophenyl)benzene (TAPB), 2,5-diethenyl-1,4-benzenedicarboxaldehyde (DVA), hydrochloric acid (HCl), thioacetamide (TAA), indium(III) chloride tetrahydrate ($InCl_3 \cdot 4H_2O$), zinc chloride ($ZnCl_2$), glycerol, triethanolamine (TEOA), and 2,2′-bipyridine (2,2′-bpy) were obtained from Aladdin Reagent Co., Ltd. All reagents used were of analytical grade and were used without further purification.

Synthesis of TAPB-COF

The TAPB-COF was synthesized with some minor modifications on the basis of the original method.[29] In a typical synthesis, 56 mg of TAPB (0.16 mmol), 44 mg of DVA (0.24 mmol), and 80 mL of MeCN were added to a 400 mL beaker. The mixture was sonicated until the two monomers were dissolved completely. Afterwards, 8 mL of HAc was added to the mixture, and stirred in a fume hood at room temperature until the solvent was almost completely volatilized. The product was collected by centrifugation and washed with ethanol three times. The obtained TAPB-DVA-COF was dispersed in 80 mL DMF. Then, 2 mL of HAc, 1.6 mL of $FeCl_3$/MeCN (50 mg mL^{-1}), and 16 mL of 3% H_2O_2 were added successively, and left for 20 min in an oven at 60 °C. The product was collected by centrifugation and washed with ethanol three times. The product was dried overnight at 60 °C. The product was labeled as TAPB-COF.

Synthesis of TAPB-COFZ-*X*

36.26 mg of TAPB-COF was added to 8 mL of H_2O and stirred for 5 min, then the pH was adjusted to 2.5 with hydrochloric acid, followed by the addition of 3 mL of glycerol and stirred for 30 min. After that, 54.5 mg of $ZnCl_2$, 117.3 mg of $InCl_3 \cdot 4H_2O$, and 60.1 mg of TAA were added to the above solution and stirred for 10 min, and then reacted in an oil bath at 80 °C for 2 h. After the reaction, the product was washed three times with water and anhydrous ethanol, centrifuged, and dried at 60 °C for 12 h. The resulting product was named TAPB-COFZ-30 (the suffix indicated the calculated weight percentage of TAPB-COF). By adjusting the amount of TAPB-COF added, with no change in the amount of other raw materials added, two other samples were added with 21.2 mg of TAPB-COF and 56.4 mg of TAPB-COF, and the resulting products were designated as TAPB-COFZ-20 and TAPB-COFZ-40, respectively.

Synthesis of ZIS

ZIS was synthesized with some minor modifications according to the previous method.[30,31] In a typical synthesis, 8 mL of H_2O was added to a 25 mL beaker and the pH was adjusted to 2.5 with hydrochloric acid; then 3 mL of glycerol was added and stirred for 3 min. After that, 54.5 mg of $ZnCl_2$, 117.3 mg of $InCl_3 \cdot 4H_2O$, and 60.1 mg of TAA were added to the above solution and stirred for 10 min, and then reacted in an oil bath at 80 °C for 2 h. After the reaction, the product was washed three times with water and anhydrous ethanol, centrifuged, and dried at 60 °C for 12 h.

Characterization

The morphology and structure of the samples were examined by field emission scanning electron microscopy (FESEM; Zeiss Sigma-500) and transmission electron microscopy (TEM; JEOL, JEM-2100). In addition, the elemental mapping images was also recorded by TEM. The crystal phases of the samples were analyzed by powder X-ray diffraction (PXRD) under Cu-Kα radiation on a Bruker D8 advanced X-ray diffractometer in the scanning ranges of 0.5°–10° and 10°–80°, respectively. X-ray photoelectron spectroscopy (XPS, EscaLab Xi^+) was used to observe the state of the surface elements using standard C 1s (284.6 eV) as a reference. UV-visible diffuse reflectance spectra (UV-vis DRS) were recorded with a Hitachi UH4150 UV-vis spectrophotometer. FTIR spectra were recorded using a Tracer-100 FT-IR spectrometer (Shimadzu Corporation). Photoluminescence (PL) spectra was obtained using a FLS980 from Edinburgh Analytical Instruments. Moreover, N_2 adsorption–desorption isotherms and CO_2 adsorption capacity were determined using a Quantachrome surface area analyzer. The specific surface area was obtained by the BET method and the pore size distribution was determined by isothermal adsorption branching. Light intensity was measured using a PL-MW 2000 photoradiometer (Perfect Light, Table S1†).

Photocatalytic CO_2 reduction

The catalyst activity was tested by photocatalytic CO_2 reduction experiments. A 60 mL reactor was charged with 5 mg of

photocatalyst, 15 mg of 2,2′-bipyridine, 2 μmol of $CoCl_2$, 1 mL of TEOA, 2 mL of H_2O, and 3 mL of MeCN, and purified with CO_2. A 300 W Xe lamp was used as the irradiation source. In each experiment, the reaction temperature was maintained at 30 °C under magnetic stirring. The concentration of the products was determined using a Foley GC970II gas chromatograph.

Photochemical testing

Photoelectrochemical experiments were carried out using a CHI660E electrochemical workstation. The test system consisted of an Ag/AgCl electrode (reference electrode), a Pt sheet (counter electrode), a photocatalyst (working electrode). The working electrode was a glassy carbon electrode (GCE) with a photocatalyst film: 15 mg of the sample was ground homogeneously, mixed with 950 μL of ethanol and 50 μL of naphthol, sonicated for 60 min, and then 10 μL of the mixture was applied to the GCE, which was dried naturally at room temperature.

Results and discussion

Photocatalyst synthesis and characterization

The synthesis route of the photocatalyst is shown in Fig. 1a. First, the TAPB-DVA-COF was synthesized by condensation reaction using TAPB and DVA as synthetic monomers; then the TAPB-COF was derived by partially breaking the imine bond, and finally, using a straightforward hydrothermal technique, the TAPB-COFZ photocatalyst was successfully created. FESEM and TEM were used to examine the appearance and morphological information of the samples. Fig. S1 and S2† show that both the TAPB-DVA-COF and TAPB-COF are roughly spherical, except that the TAPB-COF has a hollow structure. From Fig. 1, it can be seen that the TAPB-COFZ-30 photocatalyst retained the hollow spherical shape of the TAPB-COF, and the ZIS nanosheets were uniformly grown on the TAPB-COF without excessive self-assembly (Fig. 1b and c), which was favorable for exposing more active sites. In the high-resolution transmission electron microscopy (HRTEM) image (Fig. 1d), the lattice stripes with an interfacial spacing of 0.32 nm correspond to the (102) face of ZIS, which is consistent with previous reports.[16,32] The contact interface between the TAPB-COF and ZIS is indicated by the yellow dashed line, and it can be seen that the ZIS crystal face is perfectly adhered to the TAPB-COF crystal face, which indicates the successful formation of the TAPB-COFZ-30 composite (Fig. 1d). An energy dispersive X-ray detector (EDX) was used to obtain elemental mapping images (Fig. 1e). The images showed that S, In, Zn and C, N, O were well distributed in TAPB-COFZ-30, which further proved the successful formation of the TAPB-COFZ-30 composite.

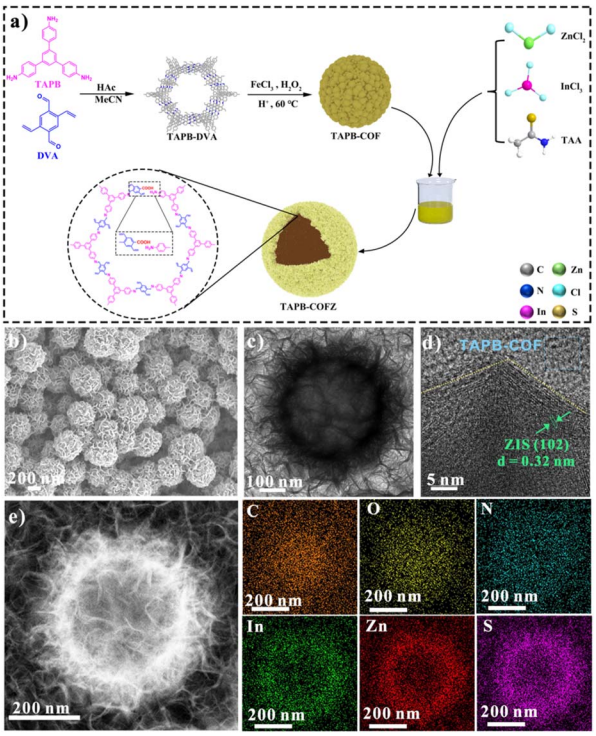

Fig. 1 (a) Synthesis route of the photocatalyst TAPB-COFZ-*X*. (b) FESEM, (c) TEM, (d) HRTEM, (e) EDX elemental mapping images of TAPB-COFZ-30.

The PXRD spectra of the prepared samples are shown in Fig. S3.† Each PXRD peak in the spectra demonstrates the high crystallinity of the TAPB-COF and the successful complexation of the photocatalyst. As shown in Fig. S3a,† there is a strong diffraction peak at 2.73°, and several weak diffraction peaks at 4.80°, 5.54°, 7.37° and 9.70°, which belong to the (100), (110), (200), (210) and (220) crystal planes of TAPB-COF, respectively. The result is consistent with previous reports,[29] indicating the successful synthesis of the TAPB-COF. With the increase in TAPB-COF content, the diffraction peaks of TAPB-COFZ-*x* (x = 20, 30, 40) at 2.73° were gradually enhanced, indicating the successful composite formation of the photocatalyst. As shown in Fig. S3b,† TAPB-COFZ-*x* (x = 20, 30, 40) perfectly inherited the diffraction peaks of ZIS and matched well with the pure hexagonal structure of ZIS (JCPDS No. 65-2023), which further indicated the successful composite formation of the photocatalyst. It is worth noting that although the diffraction peaks of the TAPB-COFZ-*X* heterostructure are very similar to those of COF and ZIS, there is a significant displacement at the peaks of COF (001) and ZIS (006). This may be due to the growth of ZIS along the COF (001) facet, and the strong interaction between the COF (001) facet and the ZIS (006) facet caused the ZIS layered structure to extend the *d*-spacing along the *c*-axis.[33]

XPS tests of the surface chemistry of pristine ZIS, TAPB-COF and TAPB-COFZ-30 were performed. In Fig. S4,† the XPS survey spectra show that the TAPB-COFZ-30 composite contains the elements C, N, O, Zn, In, and S, which is consistent with the EDX elemental mapping. As shown in Fig. 2a, the fitted peaks located at 285.95 eV and 287.7 eV are attributed to the C=N and C=O bonds in TAPB-COF. The O 1s peak binding energies located at 532.80 eV, 531.76 eV and 531 eV are attributed to the C=O, C–O bonds and absorbed oxygen in the TAPB-COF (Fig. 2b). The N 1s peak binding energies located at 400.41 eV and 399.08 eV are attributed to the C–NH_2 and C=N–C bonds in the TAPB-COF (Fig. 2c). For Zn 2p, peaks located at 1021.74 eV and 1044.77 eV are attributed to the Zn $2p_{3/2}$ and Zn $2p_{1/2}$ orbitals,[34] respectively (Fig. 2d). The two soliton rotation peaks

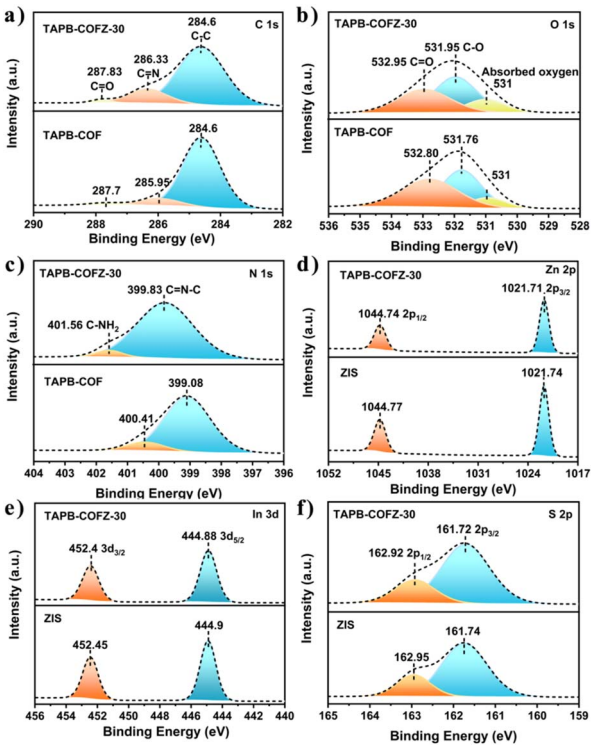

Fig. 2 High-resolution XPS spectra of TAPB-COF and TAPB-COFZ-30: (a) C 1s, (b) O 1s, (c) N 1s, (d) Zn 2p, (e) In 3d, and (f) S 2p.

in Fig. 2e are divided into $3d_{3/2}$ (452.45 eV) and $3d_{5/2}$ (444.9 eV) for In 3d in the +3 valence state.[35] In Fig. 2f, the peaks centered at 161.74 and 162.95 eV, assigned to the $2p_{2/3}$ and $2p_{1/2}$ states of S, respectively, are characteristic of S^{2-} and are in agreement with the literature.[36]

In general, the density of the atomic electron cloud is closely related to variations in the elemental binding energy. For example, the electron cloud density decreases with increasing binding energy, and the electron cloud density increases with decreasing binding energy.[37,38] This is due to the fact that the atomic electron binding energy is determined by the strong coulombic force between the outer electrons and the nucleus.[38] Hence, this shift in binding energy can be used in heterojunction catalyst systems to determine the direction of electron transfer.[39] The binding energies of C 1s, N 1s and O 1s in the TAPB-COFZ-30 composites tend to move to higher energy levels compared to those in TAPB-COF, suggesting that the incorporation of ZIS leads to a decrease in the electron cloud density of the TAPB-COF. In contrast, the binding energies of Zn 2p, In 3d, and S 2p of TAPB-COFZ-30 composites tend to move to lower energy levels compared to pure ZIS, indicating that the incorporation of TAPB-COF leads to an increase in the electron cloud density of ZIS, proving that the electrons tend to migrate from TAPB-COF to ZIS.

The characteristic functional groups of the photocatalysts were identified by FTIR. The absorption peak around 1608 cm^{-1} for the TAPB-COF is attributed to the C=N bond and is relatively weakened; besides, the absorption peaks for C=O (1662 cm^{-1}) and –OH (3355 cm^{-1}) are enhanced, suggesting that the C=N bond breaks to form –COOH (Fig. S5†).[29] In Fig. S6†, the absorption peaks about 1650 cm^{-1} and 3440 cm^{-1} in ZIS are attributed to surface-absorbed water molecules and hydroxyl groups.[40,41] Similarly, TAPB-COFZ has the same peaks, which further indicates the successful preparation of photocatalysts.

The optical absorption capabilities and electronic energy band structures of the photocatalysts were investigated using UV-vis diffuse reflectance spectroscopy (UV-vis DRS) and Mott–Schottky (M–S) measurements. As shown in Fig. S7,† ZIS shows visible absorption edges at ~500 nm, and TAPB-COF and TAPB-COFZ-x (x = 20, 30, and 40) show visible absorption fringes at ~750 nm, and the incorporation of TAPB-COF leads to a significant red shift of the absorption edges. This indicates that the composite with the TAPB-COF broadens the light absorption range of ZIS. The corresponding energy band gaps of TAPB-COF and ZIS were obtained from the Tauc plots of $(\alpha h\nu)^n$ ($n = 2$) *versus* $h\nu$. The band gap values of TAPB-COF and ZIS were 2.11 eV and 2.76 eV, respectively (Fig. S8a and b†). Generally, large absorption edges typically correspond to a narrow bandgap and potentially strong photovoltaic conversion capabilities.[42]

Positive slopes on the M–S plots of ZIS and TAPB-COF suggest that they have n-type semiconductor characteristics.[43] The CB potential of n-type semiconductors is commonly considered to be near the flat band potential.[37] Hence, from the M–S tangents (Fig. S8c and d†), the flat-band potentials of TAPB-COF and ZIS are −1.68 and −1.5 V (*vs.* Ag/AgCl, pH ~ 7), which correspond to the CB values of TAPB-COF (−1.48 V) and ZIS (−1.3 V), respectively, with respect to the normal hydrogen electrode (NHE). The CB of the photocatalyst is higher than the reduction potential required for CO_2 reduction to CO (−0.53 V *versus* NHE), which confirmed the thermodynamic feasibility of CO_2 reduction by TAPB-COFZ-30. The VB value of the samples can be defined using the equation $E_{CB} = E_{VB} - E_g$,[44] which results in 0.63 V and 1.46 V for TAPB-COF and ZIS, respectively.

Photocatalytic properties of CO_2 reduction

The CO_2 photoreduction activity of the materials was investigated in acetonitrile/water mixtures under visible light using TEOA as the electron donor and $Co(bpy)_3^{2+}$ (bpy = 2,2′-bipyridine) as the co-catalyst. As shown in Fig. 3a, the CO production rate of TAPB-COFZ-30 was measured to be 2895.94 μmol g^{-1}, apparently higher than that of ZIS (466.63 μmol g^{-1}) and TAPB-COF (87.42 μmol g^{-1}). Except for small amounts of CH_4 and H_2, no other reduction by-products were detected after the 4 h testing period (Fig. 3b), and the CO selectivity of TAPB-COFZ-30 was as high as 95.75% (Table S2†). To verify the origin of the product CO, control experiments were performed under dark conditions and without a catalyst, and no photocatalytic reduction reaction occurred, indicating that CO originated from the photocatalytic CO_2 reduction reaction driven by light irradiation. N_2 was used to replace CO_2 in the photoreduction experiment, and only a small amount of H_2 was generated, and no CO and CH_4 were generated, indicating that CO produced in the reaction originated from CO_2. In the absence of TEOA, no

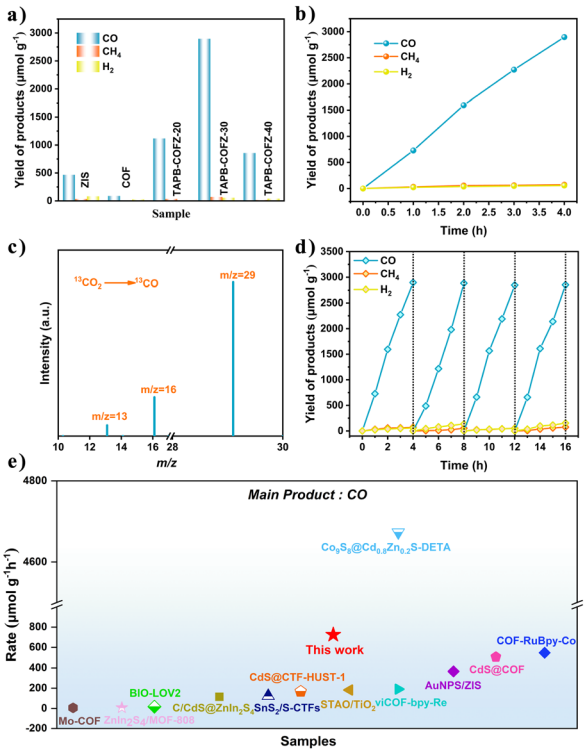

Fig. 3 (a) CO_2 photoreduction performance of different samples. (b) Time-dependent $CO/CH_4/H_2$ yields. (c) GC-MS spectrum of CO generated from the $^{13}CO_2$ isotope experiment. (d) CO_2 photoreduction stability of TAPB-COFZ-30. (e) Comparison of photocatalytic CO_2 reduction performance with recently reported photocatalysts.

obvious light attenuation process was observed. When $Co(bpy)_3^{2+}$ is not added, there are fewer photoreduction products, which indicates that $Co(bpy)_3^{2+}$ is crucial for promoting the conversion of CO_2 to CO, indirectly indicating that the main active center of photoreduction is $Co(bpy)_3^{2+}$, which is consistent with previous studies on such CO_2 photoreduction systems (Fig. S9†). Moreover, ^{13}C isotope labeling confirmed that the CO product predominantly originated from CO_2, as shown in Fig. 3c (m/z = 13, 16, 29).[45] The catalytic performance of photocatalysts for the CO_2 photoreduction reaction at different wavelengths was investigated. It can be seen from Fig. S10† that the gas evolution trend matches well with the light absorption intensity of the catalyst material, indicating that the photoexcitation of the photocatalyst triggers the CO_2 reduction reaction and realizes the generation of electric charge. Four cycles of CO_2 photoreduction experiments were carried out on TAPB-COFZ-30 under the same conditions, with each cycle lasting for 4 h, to evaluate the optical stability of the TAPB-COFZ-30 photocatalyst (Fig. 3d). The efficiency of CO generation is comparable or even higher than that of most photocatalysts reported in recent years, as shown in Fig. 3e and Table S3.†

Photochemical performance analysis

Photoelectrochemical properties are widely considered as a strong indicator of the efficiency of photogenerated charge carrier separation and migration in photocatalysts.[46] The efficacy of photogenerated carrier separation was evaluated using photoluminescence spectroscopy (PL). As shown in Fig. 4a, the PL peak intensity of TAPB-COFZ-30 is significantly lower than that of the original ZIS, implying that more electrons can participate in the photocatalytic reaction due to the inhibition of ZIS light-induced electron–hole pair recombination caused by heterojunction formation.[34] Time-resolved photoluminescence spectroscopy (TRPL) was used to further investigate the carrier dynamics of TAPB-COFZ-30 and a double-exponential kinetic function was used to fit the emission decay curve of the sample (Table S4†). As shown in Fig. 4b, the average lifetime of the pure ZIS was 1.68 ns, while the average lifetime of the TAPB-COFZ-30 composite sample increased to 2.17 ns. The significant increase in the lifetime of TAPB-COFZ-30 suggests that it effectively promotes the photo-induced separation of electrons and holes.[32] From electrochemical impedance spectroscopy (EIS), it can be seen that the semicircle of the TAPB-COFZ-30 catalyst is smaller than that of pure ZIS (Fig. 4c), which suggests that the charge transfer resistance at the electrolyte interface of TAPB-COFZ-30 is small, and interfacial charge transfer is faster.[47,48] As shown in Fig. 4d, the photocurrent of TAPB-COFZ-30 is much higher than that of ZIS, indicating that TAPB-COFZ-30 enhances the charge transfer at the interface while suppressing the compounding rate of photogenerated electrons and holes.[49]

The specific surface area of the photocatalysts as well as their CO_2 adsorption capacity are vital factors influencing photoreduction performance.[6] N_2 and CO_2 adsorption characterization of TAPB-COF, ZIS and TAPB-COFZ-30 composites was performed, and the results are shown in Fig. S11.† The specific surface area of TAPB-COF was found to be 1042.98 $m^2\ g^{-1}$, that of ZIS was 38.69 $m^2\ g^{-1}$, and that of TAPB-COFZ-30 was 196.93 $m^2\ g^{-1}$ (Fig. S11a–c†). This indicates that the incorporation of TAPB-COF effectively suppressed the agglomeration of ZIS nanosheets, increased the specific surface area of ZIS, and provided more catalytic active sites for CO_2 adsorption.

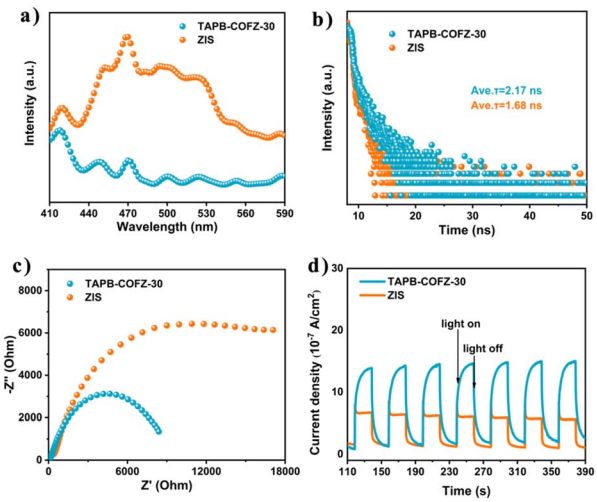

Fig. 4 (a) Steady-state PL spectra, (b) TRPL spectra of the prepared photocatalysts, (c) EIS spectra, and (d) transient photocurrent responses of ZIS and TAPB-COFZ-30.

Fig. S11d† shows the adsorption capacities of TAPB-COF, ZIS, and TAPB-COFZ-30 for CO_2, and it is evident that the incorporation of TAPB-COF increased the adsorption capacity of ZIS for CO_2, which enhanced the photocatalytic overall performance of the photocatalyst.

To further investigate the photocatalytic mechanism, the theoretical structures of the COF and ZIS were optimized and calculated. As shown in Fig. 5a and b, the density of states (DOS) indicates that C atoms dominate the COF valence and conduction band electrons, S atoms dominate the ZIS valence band electrons, and S and In atoms dominate the electron orbitals in the conduction band, respectively. Moreover, the estimated bandgaps of TAPB-COF and ZIS were found to be 1.98 eV and 2.52 eV, respectively, that are lower than our experimental results (2.11 eV and 2.76 eV). Since the accuracy of the exchange-correlation potential calculated by using density-functional theory (DFT) is limited, it is common for the calculated values to be smaller than the experimental values.[50] DFT calculations were used to investigate the electronic structure and charge transfer direction of the COF@ZIS composites, and the work function (Φ), which determines the charge transport at the interface, was obtained. As shown in Fig. 5c and d, the Φ values for COF and ZIS surfaces were 4.32 eV and 6.04 eV. The charge density distribution of the COF@ZIS heterojunction is shown in Fig. 5e, where the yellow colour represents the electron accumulation region and the cyan colour represents the electron depletion region. It can be observed that the surface of the TAPB-COF is dominated by the cyan colour, indicating charge depletion, while the surface of ZIS is dominated by a yellow colour, indicating charge accumulation. These results theoretically confirm the direction of electron transfer from the COF to ZIS.

Meanwhile, to investigate the role of the $Co(bpy)_3^{2+}$ co-catalyst in the whole photoreduction process, a steady-state fluorescence test was performed on the reaction system. As shown in Fig. S12,† the PL intensity of the mixture decreased significantly after adding $Co(bpy)_3^{2+}$ to the system, which indicated that $Co(bpy)_3^{2+}$ can inhibit the recombination of photogenerated carriers in the system.[51] At the same time, the $Co(bpy)_3^{2+}$ co-catalyst is an indispensable active site in the photoreduction process, which can be seen from previous comparative test and reports.[52,53] Moreover, DFT calculations also showed that $Co(bpy)_3^{2+}$ can spontaneously adsorb on the surface of ZIS (Fig. S13†).

In order to deeply explore the reaction intermediates in the photocatalytic carbon dioxide reduction process, we carried out *in situ* FTIR spectroscopic studies. As shown in Fig. 6a, there were no obvious characteristic peaks before light exposure, while a series of intermediate peaks appeared after light exposure. With increasing irradiation time, the peaks included HCO_3^- (1435, 1688, 1783 cm^{-1}),[40,54,55] m-CO_3^{2-} (1283, 1513 cm^{-1}),[56,57] b-CO_3^{2-} (1356, 1585, 1660 cm^{-1}),[40,58,59] and CO_2^- (1708 cm^{-1}),[60] indicating absorption and activation of CO_2 and H_2O onto the photocatalyst. Characteristic peaks of *COOH can also be found, which is usually considered the key intermediate for CO_2 reaction to CO or methane (1530, 1550, 1570, and 1633 cm^{-1}).[54–56,61–63] The peak at 2078 cm^{-1} belongs to *CO and marks the formation of the final product.[64] In addition, the photoreduction mechanisms of ZIS and TAPB-COFZ-30 were further investigated by Gibbs free energy calculations. Based on the *in situ* FTIR results of TAPB-COFZ-30, it is presumed that the photoreduction reaction proceeds through CO_2(g), *+CO_2, *COOH, *CO, and *+CO(g) (Fig. 6b and S14–S18†). The DFT

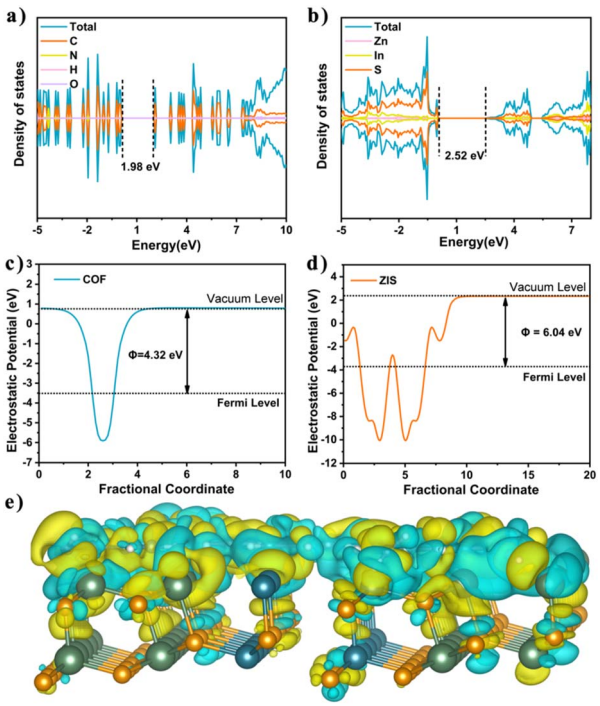

Fig. 5 (a) TAPB-COF, (b) ZIS density of states (DOS), (c) TAPB-COF, (d) ZIS surfaces for the work function, and (e) average charge density difference for TAPB-COFZ-30.

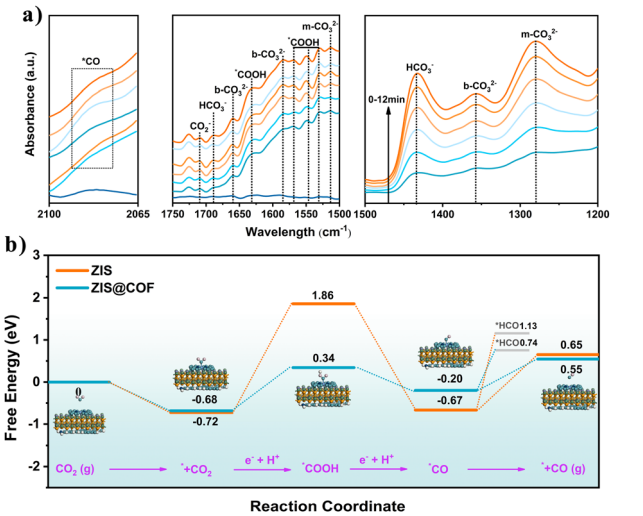

Fig. 6 (a) *In situ* FTIR spectra of the photoreduction process of CO_2 on TAPB-COFZ-30 under different irradiation times. (b) Gibbs free energy diagrams of CO_2 reduction to CO for ZIS and TAPB-COFZ-30 photocatalysts. ("*" represents adsorption on the substrate; the figure shows the calculation model of TAPB-COFZ-30 adsorption energy).

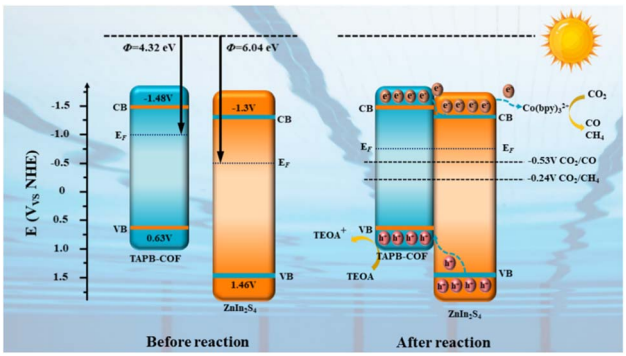

Fig. 7 Proposed reaction mechanism for photocatalytic CO_2 reduction on the TAPB-COFZ-30 hollow core–shell heterojunction.

results show that the formation of *COOH has the highest energy barrier, suggesting that this step is the rate-limiting step for the photoreduction of CO_2 to CO.[65] Among them, TAPB-COFZ-30 generates *COOH with a ΔG of 1.02 eV, which is much lower than that of ZIS (ΔG = 2.58 eV). It demonstrated that the creation of the heterojunction was useful for optimizing the rate-limiting step, thus accelerating the CO_2 reduction reaction kinetics. In addition, TAPB-COFZ-30 exhibited a lower energy barrier than pure ZIS in the step from *CO to *+CO(g), suggesting that CO is more easily desorbed from TAPB-COFZ-30. From the results of the ΔG calculations above, it can be shown that the formation of the heterojunction can decrease the reaction energy barrier during the CO_2 photoreduction process, which is one of the important reasons for TAPB-COFZ-30's improved photocatalytic performance for CO_2 reduction to CO. Moreover, the calculations show that the Gibbs free energy for generating *HCO from *CO is greater than that for generating CO(g), which explains the high selectivity for the reduction of CO_2 to CO.

Therefore, a type-II transfer mechanism (Fig. 7) at the TAPB-COFZ heterojunction interface is proposed after combining our previously described experimental results and theoretical calculations on the charge transfer dynamics between the two energy levels of COF@ZIS. The potential difference resulting from the different work functions of COF and ZIS drives the electrons to diffuse from the COF to ZIS, resulting in ZIS acquiring electrons, whereas the COF becomes electron-deficient. Meanwhile, the trapping of holes by the sacrificial agent TEOA on the VB of the COF can effectively avoid the occurrence of reversible reactions, which makes it easier to separate the photogenerated electrons and holes; CO_2 is reduced to CO in the presence of ZIS and co-catalysts.

Conclusions

By *in situ* growth of ZIS on the surface of hollow TAPB-COF nanospheres, TAPB-COFZ heterojunctions with hollow core–shell structures were constructed. For the photocatalyst, the nitrogen-rich TAPB-COF can effectively adsorb and activate CO_2, while the heterojunction interface effectively promotes carrier separation and transfer. The TAPB-COFZ photocatalysts exhibited an efficient CO_2 reduction rate and excellent stability in the water/acetonitrile (H_2O/MeCN) tandem system. The key *COOH intermediate in the conversion of CO_2 to CO was confirmed by *in situ* FTIR and density-functional theory calculations, further supporting the proposed reaction mechanism. This work bridges the research on COF@ZIS heterojunctions for CO_2 reduction and may encourage the development of photocatalysts with more desirable COF heterojunction-based photocatalysts, as well as the coupling of molecular co-catalysts for efficient CO_2 photo-fixation.

Data availability

The data supporting this article have been included as part of the ESI.†

Author contributions

Hui-Tao Fan: conceptualization, lead; data curation, equal; supervision, lead; visualization, lead; writing – original draft, lead; writing – review & editing, lead. Minglin Hu: data curation, supporting; formal analysis, lead; investigation, equal; methodology, equal; writing – original draft, equal. Yabing Duan: data curation, equal; investigation, equal; methodology, equal. Luyang Zuo: investigation, equal; software, lead. Ronggui Yu: data curation, supporting; investigation, equal. Zhuwei Li: investigation, supporting; methodology, supporting. Qi Liu: data curation, equal; formal analysis, equal; investigation, equal. Bo Li: funding acquisition, lead; resources, lead; supervision, equal. Liya Wang: supervision, equal; writing – review & editing, equal.

Conflicts of interest

There are no conflicts to declare.

Acknowledgements

This work was supported by the Program for Science and Technology Innovation Talents in Universities of Henan Province (No. 22HASTIT007), and the Special Foundation of Nanyang Normal University (2024ZX004).

References

1 S. Chu and A. Majumdar, *Nature*, 2012, **488**, 294–303.
2 P. Prabhu, V. Jose and J. M. Lee, *Adv. Funct. Mater.*, 2020, **30**, 1910768.
3 A. R. Woldu, P. Talebi, A. G. Yohannes, J. Xu, X. D. Wu, S. Siahrostami, L. Hu and X. C. Huang, *Angew. Chem., Int. Ed.*, 2023, **62**, e202301621.
4 Q. Wang and K. Domen, *Chem. Rev.*, 2019, **120**, 919–985.
5 X. Lin, S. Xia, L. Zhang, Y. Zhang, S. Sun, Y. Chen, S. Chen, B. Ding, J. Yu and J. Yan, *Adv. Mater.*, 2022, **34**, 2200756.
6 G. Zhang, X. Li, D. Chen, N. Li, Q. Xu, H. Li and J. Lu, *Adv. Funct. Mater.*, 2023, **33**, 2308553.

7 Y. Feng, C. Wang, P. Cui, C. Li, B. Zhang, L. Gan, S. Zhang, X. Zhang, X. Zhou, Z. Sun, K. Wang, Y. Duan, H. Li, K. Zhou, H. Huang, A. Li, C. Zhuang, L. Wang, Z. Zhang and X. Han, *Adv. Mater.*, 2022, **34**, 2109074.
8 F. Chen, Z. Ma, L. Ye, T. Ma, T. Zhang, Y. Zhang and H. Huang, *Adv. Mater.*, 2020, **32**, 1908350.
9 K. Guo, X. Zhu, L. Peng, Y. Fu, R. Ma, X. Lu, F. Zhang, W. Zhu and M. Fan, *Chem. Eng. J.*, 2021, **405**, 127011.
10 A. Nakada, H. Kumagai, M. Robert, O. Ishitani and K. Maeda, *Acc. Mater. Res.*, 2021, **2**, 458–470.
11 R. T. Guo, X. Hu, X. Chen, Z. X. Bi, J. Wang and W. G. Pan, *Small*, 2023, **19**, 2207767.
12 T. Inoue, A. Fujishima, S. Konishi and K. Honda, *Nature*, 1979, **277**, 637–638.
13 C. Dong, C. Lian, S. Hu, Z. Deng, J. Gong, M. Li, H. Liu, M. Xing and J. Zhang, *Nat. Commun.*, 2018, **9**, 1252.
14 C. Gao, T. Wei, Y. Zhang, X. Song, Y. Huan, H. Liu, M. Zhao, J. Yu and X. Chen, *Adv. Mater.*, 2019, **31**, 1806596.
15 H. Ou, L. Lin, Y. Zheng, P. Yang, Y. Fang and X. Wang, *Adv. Mater.*, 2017, **29**, 1700008.
16 H. Fan, Y. Jin, K. Liu and W. Liu, *Adv. Sci.*, 2022, **9**, 2104579.
17 X. Zheng, Y. Song, Y. Liu, Y. Yang, D. Wu, Y. Yang, S. Feng, J. Li, W. Liu, Y. Shen and X. Tian, *Coord. Chem. Rev.*, 2023, **475**, 214898.
18 W. Yang, L. Zhang, J. Xie, X. Zhang, Q. Liu, T. Yao, S. Wei, Q. Zhang and Y. Xie, *Angew. Chem., Int. Ed.*, 2016, **55**, 6716–6720.
19 Y. Pan, X. Yuan, L. Jiang, H. Yu, J. Zhang, H. Wang, R. Guan and G. Zeng, *Chem. Eng. J.*, 2018, **354**, 407–431.
20 G. Zuo, Y. Wang, W. L. Teo, A. Xie, Y. Guo, Y. Dai, W. Zhou, D. Jana, Q. Xian, W. Dong and Y. Zhao, *Angew. Chem., Int. Ed.*, 2020, **59**, 11287–11292.
21 G. Zuo, Y. Wang, W. L. Teo, Q. Xian and Y. Zhao, *Appl. Catal., B*, 2021, **291**, 120126.
22 S. Wang, Y. Wang, S. L. Zhang, S. Q. Zang and X. W. Lou, *Adv. Mater.*, 2019, **31**, 1903404.
23 S. Chandra, T. Kundu, S. Kandambeth, R. BabaRao, Y. Marathe, S. M. Kunjir and R. Banerjee, *J. Am. Chem. Soc.*, 2014, **136**, 6570–6573.
24 H. Ma, B. Liu, B. Li, L. Zhang, Y.-G. Li, H.-Q. Tan, H.-Y. Zang and G. Zhu, *J. Am. Chem. Soc.*, 2016, **138**, 5897–5903.
25 A. P. Côté, A. I. Benin, N. W. Ockwig, M. O'Keeffe, A. J. Matzger and O. M. Yaghi, *Science*, 2005, **310**, 1166–1170.
26 H. M. El-Kaderi, J. R. Hunt, J. L. Mendoza-Cortés, A. P. Côté, R. E. Taylor, M. O'Keeffe and O. M. Yaghi, *Science*, 2007, **316**, 268–272.
27 H. Furukawa and O. M. Yaghi, *J. Am. Chem. Soc.*, 2009, **131**(25), 8875–8883.
28 Y. Zeng, R. Zou and Y. Zhao, *Adv. Mater.*, 2016, **28**, 2855–2873.
29 S. Liu, K. Dou, B. Liu, M. Pang, P. a. Ma and J. Lin, *Angew. Chem., Int. Ed.*, 2023, **62**, e202301831.
30 S. Wang, B. Y. Guan and X. W. D. Lou, *J. Am. Chem. Soc.*, 2018, **140**, 5037–5040.
31 M. Zhou, S. Li, S. Wang, Z. Jiang, C. Yang, F. Guo, X. Wang and W.-K. Ho, *Appl. Surf. Sci.*, 2022, **599**, 153985.
32 S. Wang, B. Y. Guan, X. Wang and X. W. D. Lou, *J. Am. Chem. Soc.*, 2018, **140**, 15145–15148.
33 C. Cui, X. Xu, X. Zhao, N. Xi, M. Li, X. Wang, Y. Sang, X. Yu, H. Liu and J. Wang, *Nano Energy*, 2024, **126**, 109632.
34 C. Q. Li, X. Du, S. Jiang, Y. Liu, Z. L. Niu, Z. Y. Liu, S. S. Yi and X. Z. Yue, *Adv. Sci.*, 2022, **9**, 2201773.
35 S. Lu, S. Zhang, L. Li, C. Liu, Z. Li and D. Luo, *Chem. Eng. J.*, 2024, **483**, 149058.
36 X. Jia, Y. Lu, K. Du, H. Zheng, L. Mao, H. Li, Z. Ma, R. Wang and J. Zhang, *Adv. Funct. Mater.*, 2023, **33**, 2304072.
37 S. Bao, Q. Tan, S. Wang, J. Guo, K. Lv, S. A. C. Carabineiro and L. Wen, *Appl. Catal., B*, 2023, **330**, 122624.
38 P. Zhang, Y. Li, Y. Zhang, R. Hou, X. Zhang, C. Xue, S. Wang, B. Zhu, N. Li and G. Shao, *Small Methods*, 2020, **4**, 2000214.
39 J. Low, B. Dai, T. Tong, C. Jiang and J. Yu, *Adv. Mater.*, 2019, **31**, 1802981.
40 M. Song, X. Song, X. Liu, W. Zhou and P. Huo, *Chin. J. Catal.*, 2023, **51**, 180–192.
41 M. Zhou, S. Wang, P. Yang, Z. Luo, R. Yuan, A. M. Asiri, M. Wakeel and X. Wang, *Chem.–Eur. J.*, 2018, **24**, 18529–18534.
42 M. Liu, Y. Ning, M. Ren, X. Fu, X. Cui, D. Hou, Z. Wang, J. Cui and A. Lin, *Small*, 2023, **19**, 2303876.
43 P. Xia, S. Cao, B. Zhu, M. Liu, M. Shi, J. Yu and Y. Zhang, *Angew. Chem., Int. Ed.*, 2020, **59**, 5218–5225.
44 T. Zhang, F. Meng, M. Gao, W. L. Ong, K. G. Haw, T. Ding, G. W. Ho and S. Kawi, *EcoMat*, 2021, **3**, e12152.
45 S. Wang, X. Hai, X. Ding, S. Jin, Y. Xiang, P. Wang, B. Jiang, F. Ichihara, M. Oshikiri, X. Meng, Y. Li, W. Matsuda, J. Ma, S. Seki, X. Wang, H. Huang, Y. Wada, H. Chen and J. Ye, *Nat. Commun.*, 2020, **11**, 1149.
46 K. Dai, L. Lu, C. Liang, Q. Liu and G. Zhu, *Appl. Catal., B*, 2014, **156–157**, 331–340.
47 Y. Zheng, J. Dong, C. Huang, L. Xia, Q. Wu, Q. Xu and W. Yao, *Appl. Catal., B*, 2020, **260**, 118220.
48 Z. Lin, C. Shao, S. Jiang, C. Sun and S. Song, *Appl. Catal., B*, 2020, **268**, 118742.
49 Z. Wang, Y. Chen, L. Zhang, B. Cheng, J. Yu and J. Fan, *J. Mater. Sci. Technol.*, 2020, **56**, 143–150.
50 M. Dong, P. Zhou, C. Jiang, B. Cheng and J. Yu, *Chem. Phys. Lett.*, 2017, **668**, 1–6.
51 R. Wang, P. Yang, S. Wang and X. Wang, *J. Catal.*, 2021, **402**, 166–176.
52 B. Su, H. Huang, Z. Ding, M. B. J. Roeffaers, S. Wang and J. Long, *J. Mater. Sci. Technol.*, 2022, **124**, 164–170.
53 L. Huang, B. Li, B. Su, Z. Xiong, C. Zhang, Y. Hou, Z. Ding and S. Wang, *J. Mater. Chem. A*, 2020, **8**, 7177–7183.
54 Y. Zhang, J. Li, W. Zhou, X. Liu, X. Song, S. Chen, H. Wang and P. Huo, *Appl. Catal., B*, 2024, **342**, 123449.
55 Y. Zhang, M. Xu, W. Zhou, X. Song, X. Liu, J. Zhang, S. Chen and P. Huo, *J. Colloid Interface Sci.*, 2023, **650**, 1762–1772.
56 S. Si, H. Shou, Y. Mao, X. Bao, G. Zhai, K. Song, Z. Wang, P. Wang, Y. Liu, Z. Zheng, Y. Dai, L. Song, B. Huang and H. Cheng, *Angew. Chem., Int. Ed.*, 2022, **61**, e202209446.
57 J. Wang, L. Huang, B. Sun, H. Zhang, D. Hou, X.-q. Qiao, H. Ma and D.-S. Li, *Chem. Eng. J.*, 2024, **479**, 147719.

58 Y. He, C. Chen, Y. Liu, Y. Yang, C. Li, Z. Shi, Y. Han and S. Feng, *Nano Lett.*, 2022, **22**, 4970–4978.
59 H. Wang, J. Li, Y. Wan, A. Nazir, X. Song, P. Huo and H. Wang, *Appl. Surf. Sci.*, 2023, **613**, 155989.
60 C.-L. Tan, M.-Y. Qi, Z.-R. Tang and Y.-J. Xu, *ACS Catal.*, 2023, **13**, 8317–8329.
61 F. Wang, T. Hou, X. Zhao, W. Yao, R. Fang, K. Shen and Y. Li, *Adv. Mater.*, 2021, **33**, 2102690.
62 X. Li, Y. Sun, J. Xu, Y. Shao, J. Wu, X. Xu, Y. Pan, H. Ju, J. Zhu and Y. Xie, *Nat. Energy*, 2019, **4**, 690–699.
63 S. Karmakar, S. Barman, F. A. Rahimi and T. K. Maji, *Energy Environ. Sci.*, 2021, **14**, 2429–2440.
64 X. Yi, S. Zhang, H. Shen, B. Li, L. Yang, W. Dai, R. Song, J. Zou and S. Luo, *Appl. Catal., B*, 2023, **338**, 123003.
65 B. Su, M. Zheng, W. Lin, X. F. Lu, D. Luan, S. Wang and X. W. Lou, *Adv. Energy Mater.*, 2023, **13**, 2203290.